Nemo-Nordic 2.0: Operational marine forecast model for the Baltic Sea

Tuomas Kärnä[1], Patrik Ljungemyr[2], Saeed Falahat[2], Ida Ringgaard[3], Lars Axell[2], Vasily Korabel[3], Jens Murawski[3], Ilja Maljutenko[4], Anja Lindenthal[5], Simon Jandt-Scheelke[5], Svetlana Verjovkina[4], Ina Lorkowski[5], Priidik Lagemaa[4], Jun She[3], Laura Tuomi[1], Adam Nord[2], and Vibeke Huess[3]

[1]Finnish Meteorological Institute, Helsinki, Finland
[2]Swedish Meteorological and Hydrological Institute, Norrköping, Sweden
[3]Danish Meteorological Institute, Copenhagen, Denmark
[4]Tallinn University of Technology, Tallinn, Estonia
[5]Bundesamt für Seeschifffahrt und Hydrographie, Hamburg, Germany

Correspondence: Tuomas Kärnä (tuomas.karna@fmi.fi)

1   **Abstract.** This paper describes Nemo-Nordic 2.0, an operational marine model for the Baltic Sea. The model is used for both
2   near-real-time forecasts as well as hindcast purposes. It provides estimates of sea surface height, water temperature, salinity and
3   velocity as well as sea ice concentration and thickness. The model is based on the NEMO (Nucleus for European Modelling
4   of the Ocean) circulation model and the previous Nemo-Nordic 1.0 configuration by Hordoir et al. [Geosci. Model Dev., 12,
5   363–386, 2019]. The most notable updates include the switch from NEMO version 3.6 to 4.0, updated model bathymetry and
6   revised bottom friction formulation. The model domain covers the Baltic and the North Seas with approximately 1 nautical
7   mile resolution. Vertical grid resolution has been increased from 3 to 1 m in the surface layer. In addition, the numerical solver
8   configuration has been revised to reduce artificial mixing to improve the representation of inflow events. Sea-ice is modeled
9   with the SI3 model instead of LIM3. The model is validated against sea level, water temperature, and salinity observations, as
10   well as Baltic Sea ice chart data for a two-year hindcast simulation (October 2014 to September 2016). Sea level root mean
11   square deviation (RMSD) is typically within 10 cm throughout the Baltic basin. Seasonal sea surface temperature variation
12   is well captured, although the model exhibits a negative bias of approximately -0.5°C. Salinity RMSD is typically below 1.5
13   g/kg. The model captures the 2014 Major Baltic Inflow event and its propagation to the Gotland Deep. The model assessment
14   demonstrates that Nemo-Nordic 2.0 can reproduce the hydrographic features of the Baltic Sea.

1   Introduction

16   The Baltic Sea is a brackish, semi-enclosed water body in the northern Europe (Figure 1). It has unique characteristics due to
17   large freshwater input and restricted water exchange with the North Sea. Several ocean circulation models have been set up
18   for the Baltic Sea with varying configurations (e.g., Lehmann, 1995; Meier et al., 1999; Funkquist and Kleine, 2007; Berg and
19   Poulsen, 2012; Dietze et al., 2014; Gräwe et al., 2015a; Hordoir et al., 2019).

20   Operational ocean modeling has a fairly long history in the Baltic Sea, starting already in the mid 1990s with HIROMB (High
21   Resolution Operational Model for the Baltic). It was a cooperation involving many Baltic institutes who gathered around a

common circulation model with the same name. The cooperation itself later became the modeling part of the Baltic Operational Oceanographic System (BOOS; https://boos.org; She et al. 2020), or the BOOS Modelling Programme. The HIROMB model itself existed in several branches in different institutes for many years, e.g. the HIROMB model (Funkquist and Kleine, 2007; Axell, 2013) at the Swedish Meteorological and Hydrological Institute (SMHI), and the HIROMB BOOS Model (HBM; Berg and Poulsen 2012). The first version of a common ocean circulation model built around the Nucleus for European Modelling of the Ocean (NEMO) was called Nemo-Nordic 1.0 and was described and validated by Pemberton et al. (2017) and Hordoir et al. (2019). It was based on NEMO version 3.6 and was coupled to the integrated ice model LIM3 (Vancoppenolle et al., 2009).

In this paper, we present an updated Nemo-Nordic 2.0 model for the Baltic Sea based on the NEMO circulation model version 4.0 (Madec et al. 2019). The model domain covers the North and Baltic Seas (Fig. 1). The setup is based on the Nemo-Nordic 1.0 configuration (Hordoir et al., 2019). Compared to Nemo-Nordic 1.0, most notable updates are the switch from NEMO 3.6 to NEMO 4.0, updated bathymetry and revised bottom friction formulation. Vertical grid resolution has been increased in the surface layer from 3 to 1 m. We have also revised the numerical schemes (e.g. advection of momentum and tracers) to reduce artificial mixing. Finally, NEMO 4.0 uses the SI3 sea ice model instead of LIM3.

Modeling the circulation in the Baltic Sea is challenging due to the complex topography, strong stratification, and dense inflows related to the Major Baltic Inflow (MBI) events (Mohrholz et al., 2015; Gräwe et al., 2015b; Mohrholz, 2018). Due to the complex non-linear interaction with the North Sea (Gustafsson, 1997; Gustafsson and Andersson, 2001), it is widely accepted that the North and Baltic Seas must be modeled as a single, coupled system (Daewel and Schrum, 2013; Pätsch et al., 2017; Hordoir et al., 2019). Water exchange in the system is governed by the fluxes between the sub-basins. Many constraining regions, such as the Danish Straits or the Archipelago Sea, are characterized by fine-scale bathymetric features that are difficult to resolve in operational models. Representing the Danish Straits region, for example, requires sub-kilometer scale horizontal resolution (She et al., 2007; Gräwe et al., 2015a; Stanev et al., 2018).

Salt pulses propagate as a density-driven bottom current from basin to basin. In circulation models, artificial numerical mixing can slow down or completely arrest the propagation of the current (Hofmeister et al., 2011; Klingbeil et al., 2014). Spurious vertical mixing can also cause excessive ventilation of the oxygen-depleted deep waters (Rennau and Burchard, 2009). In finite volume models, the accuracy of the advection scheme has a significant impact on the level of numerical mixing (Zalesak, 1979; Hourdin and Armengaud, 1999; Lévy et al., 2001; Klingbeil et al., 2014). Previous studies suggest that vertical grid resolution plays an important role in retaining the salt pulse density structure in the Baltic Sea (Hofmeister et al., 2011; Gräwe et al., 2015a).

The aim of this article is to validate the Nemo-Nordic 2.0 model configuration. The configuration is used in the EU Copernicus Marine Service for both near-real-time forecasts, as well as multi-year hindcast simulations for the Baltic Sea. The presented validation is based on a 2-year hindcast simulation that uses similar forcing as the operational configuration. The presented validation run uses a 3 km DMI HIRLAM atmospheric forcing whereas the operational model will use 2.5 km Met-CoOP HARMONIE model forecast padded with ECMWF HRES forecast data in North Sea regions outside the MetCoOP domain.
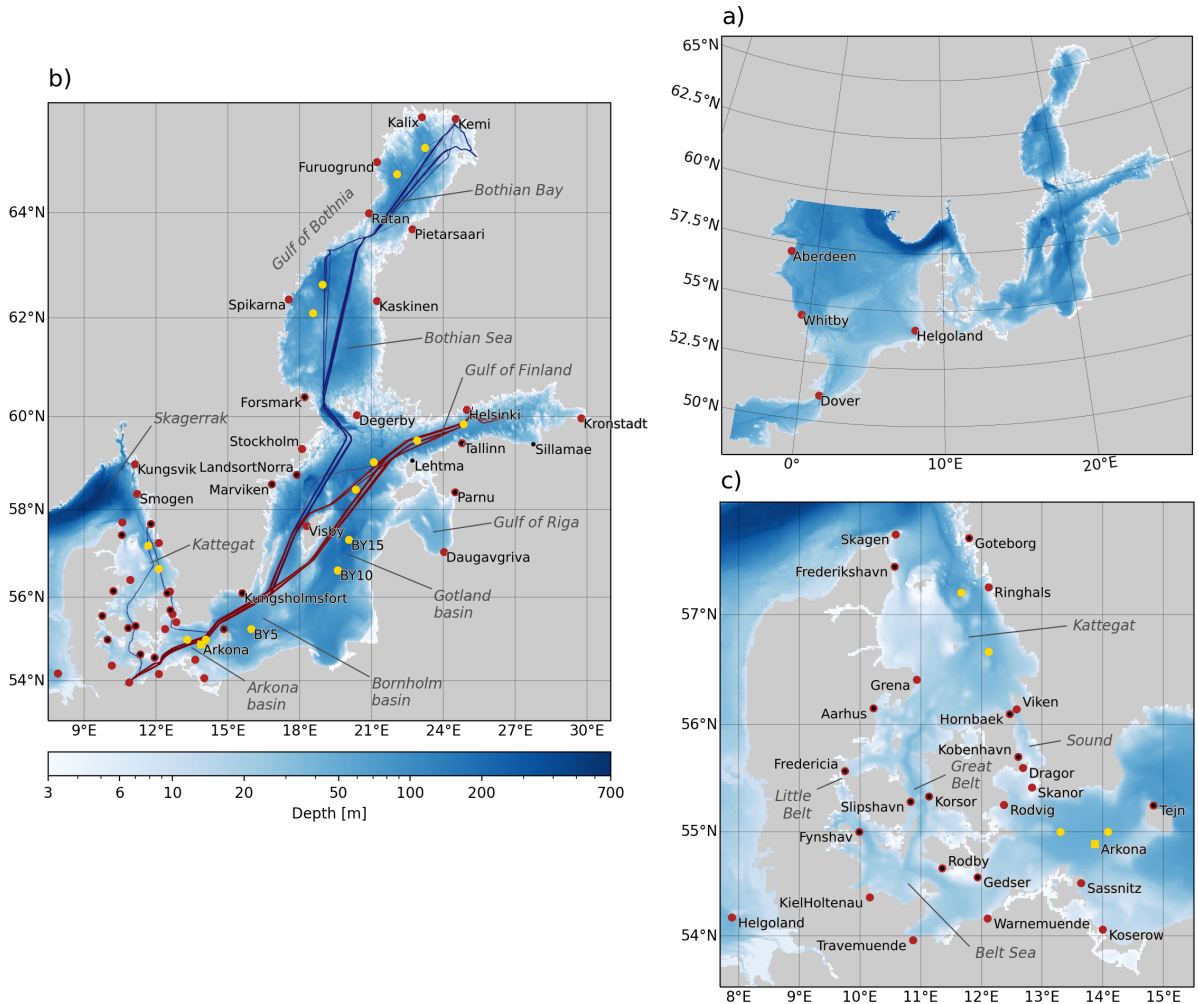
Figure 1. Computational domain and bathymetry; a) the entire model domain, b) the Baltic Sea, c) Danish Straits region. Red and black dots indicate station locations with SSH and SST observations, respectively; Yellow dots indicate vertical profile locations. Blue and red lines illustrate the TransPaper and FinnMaid ferry routes, respectively.

The model skill is assessed with respect to variables that are of interest to the users: sea surface height (SSH), water temperature and salinity, as well as sea ice coverage using observations. Observational data from tide gauges, FerryBox instruments, vertical profiles, as well as ice charts is used. The model configuration and used observation data sets are presented in Section 2. Section 3 presents the model assessment metrics, followed by a discussion and conclusions in Section 4.

2 Methods

2.1 Model domain and configuration

The presented model setup is an updated version of the Nemo-Nordic 1.0 configuration (Hordoir et al., 2019) implemented on NEMO version 4.0 (Madec et al. 2019; subversion repository revision 11281). Compared to Nemo-Nordic 1.0, the main improvements are the updated NEMO model version, switching from the LIM3 sea ice model to SI3, updated model bathymetry and land mask, revised bottom friction formulation, revised vertical grid, and revised solver options to reduce numerical mixing.

The grid covers the North and Baltic Seas, spanning from 4.15278°W to 30.18021°E and 48.4917°N to 65.8914216°N (Figure 1 a). The horizontal grid resolution is 0.0277775° and 0.0166664° in the zonal and meridional directions, respectively, resulting in approximately 1 nautical mile resolution. In the North Sea, the open boundaries are located in the western part of the English Channel and between Scotland and Norway.

The model uses a z^* grid in the vertical direction, consisting of 56 levels. The layer thickness is 1 m at the surface, increasing to 10 m at 75 m depth, and maximum 24 m at 700 m depth. In the bottom cell a partial step formulation is used, i.e. the location of the bottom node is fitted to the local bathymetry instead of fixing it to the full z level height.

The model's bathymetry is derived from the global GEBCO data set (the GEBCO-2014 grid, version 20150318; http://www.gebco.net, last access: March 29, 2021). The data were interpolated to the centroids of the model grid. The land mask was generated from OpenStreetMap coastline data (https://www.openstreetmap.org, last access: March 29, 2021) and the GEBCO bathymetry. In the Baltic Sea, the minimum depth was set to 3 m. In the North Sea, the minimum depth varies between 5 and 10 m to accommodate tidal variations as wetting and drying is not used. The bathymetry was modified along the west coast of Denmark by masking out shallow lagoons and channels (such as the Wadden Sea, Ringkøbing Fjord and Limfjord area; cut-off depth was 10 m; Fig 1 c) to improve the propagation of tides to Skagerrak and Kattegat. Furthermore, to improve the inflow of salt water into the Baltic Sea, the bathymetry was modified in the Danish Straits region (see Sect. 2.2).

The model configuration was tuned to accurately simulate surface gravity waves and internal gravitational currents. Bottom friction is imposed with implicit nonlinear log-layer parameterization. The bottom drag, C_d, was computed from a spatially variable bottom roughness length parameter, z_0^b,

$$C_d = \left(\frac{\kappa}{\log \left(\frac{z_0^b + h_0/2}{z_0^b} \right)} \right)^2 , \tag{1}$$

where h_0 is height of the bottom cell, and κ is the von Karman constant. As NEMO 4.0 only allows users to specify the C_d field directly, the formulation (1) was implemented in NEMO, introducing a user-defined z_0^b field. With the z^* vertical coordinates, the cell height varies in time, and consequently C_d becomes time dependent. The bottom roughness length formulation (1) is consistent with the law of the wall boundary layer theory, and it is the preferred parameterization especially in coastal and shallow regions. The additional benefit is that, unlike C_d, z_0^b does not depend on the cell height, making the configuration more robust with respect to changes in the vertical grid and bathymetry.

92   The bottom roughness field was tuned to improve sea level skill throughout the model domain. In the English Channel z_0^b

93   was set to 0.3 mm to avoid dampening the tidal signal along the continental coast. In the northwestern part of the North Sea

94    $z_0^b = 1$ cm and $z_0^b = 3$ cm in the Danish Straits to introduce sufficient dissipation. In the Baltic Sea, 1 mm was used to prevent

95   excessive damping of seiche motions.

96   We use a non-linear free surface formulation with mode-splitting. The baroclinic and barotropic time steps are 90 and 3 s,

97   respectively. Model outputs were stored at 1 h resolution. Fast variations in the 2D fields are filtered out by averaging over

98   two baroclinic time steps. A vector-invariant form of the momentum equation is used with an energy and enstrophy conserving

99   advection scheme. This choice improves the representation of baroclinic eddies, reduces noise in the velocity field and also

100   improves the interaction of currents and topography in partial step configurations (Madec et al., 2019).

101   Vertical turbulence is modeled with the Generic Length Scale model (Umlauf and Burchard, 2003; Reffray et al., 2015),

102   using $k - \varepsilon$ closure and Canuto A stability functions. Horizontal diffusion of momentum and tracers were modeled with a

103   Laplacian formulation with constant-in-time diffusivity and viscosity. In the surface layer (top 10 m), viscosity and diffusivity

104   were set to 50 and 5 m^2 s^{-1}, respectively. For the rest of the water column, horizontal viscosity was 0.01 m^2 s^{-1} and diffusivity

105   was neglected to avoid excessive mixing in the bottom layer (Hordoir et al., 2019).

106   In NEMO 4.0, we use the TEOS-10 equation of state (IOC, 2010; Roquet et al., 2015) to compute water density. Conse-

107   quently, the modeled water salinity and temperature are in Absolute Salinity (g/kg) and Conservative Temperature (°C) units,

108   respectively. When comparing against observations, the model's temperature is converted to in-situ temperature.

109   Sea-ice dynamics are modeled with the SI3 sea-ice model. SI3 solves the sea-ice thermodynamics, advection, rheology and

110   ridging/rafting. The landfast ice parametrization by Lemieux et al. (2016) is used. The model consist of five ice categories and

111   one snow category. Ice thickness categories are defined with the thickness bounds 0.45, 1.13, 2.14, and 3.67 m. In this work,

112   we use the standard settings in the sea-ice model, originally developed for the global ocean, for the ice thickness categories;

113   Further tuning of the configuration for the Baltic Sea will be performed at a later stage.

114   ## 2.2   Improving salinity inflows

115   Salt water inflows to the Baltic Sea are extremely sensitive to bathymetric features, especially in the Danish Straits region, and

116   numerical aspects of the model. To improve the representation of the inflow events, the bathymetry in the Danish Straits area

117   was tuned. It is known that the narrow channels in the Straits (the Little Belt, Great Belt, and the Sound; Fig. 1c) play a crucial

118   role in the water exchange between the North Sea and the Baltic Sea by allowing dense waters to creep to the Arkona basin.

119   These channels are, however, very narrow and resolving them properly would require a much finer grid resolution (approxi-

120   mately 250 m; e.g., Stanev et al. 2018) than what is feasible in an operational model of the presented extent. Consequently, in

121   coarser resolution configurations, the bathymetry must be tuned to facilitate the influx of dense water masses (e.g., She et al.,

122   2007).

123   First, the bathymetry in the Great Belt was artificially deepened by a factor of 1.3 to allow the influx of dense waters. Next,

124   the bathymetry was smoothed in the Danish Straits region between Kattegat and the Arkona basin by applying a Gaussian

125   filter on the bathymetry raster field (using standard deviation σ of 2 grid cells). Large local gradients in the bathymetry field

126 introduces local obstructions ("sills") and also generates noise in the velocity field which tends to mix the tracers and thus

127 reduce the pressure gradient driving the gravitational current. A less intrusive smoothing (a Gaussian filter with $\sigma = 0.66$) was

128 applied in the rest of the Baltic basin; our test runs indicate that a smoother bathymetry improves otherwise underestimated sea

129 level variability in coastal regions, e.g. in the Gulf of Bothnia. Both the smoothing and deepening of the local bathymetry were

130 necessary to reproduce Major Baltic Inflow events in the model.

131 In finite volume models, the accuracy of tracer and momentum advection schemes has a great impact on the effective

132 numerical dissipation of the model. In the baroclinic regime, numerical models tend to generate noise at grid scale in the

133 velocity field which tends to increase artificial mixing of tracers. Griffies and Hallberg (2000) and Ilıcak et al. (2012) have

134 demonstrated that adding a suitable amount of viscosity can effectively suppress such oscillations in the velocity field, and

135 therefore reduce the overall mixing of tracers. Moreover, higher order advection schemes can be utilized to reduce numerical

136 mixing but they can also generate spurious, unphysical, oscillations in the advected quantity. In this work, we have chosen to

137 use the 3rd order Upstream Biased Scheme (UBS), and the 4th order centered scheme, for horizontal and vertical advection

138 of momentum, respectively. The same advection scheme combination is used in ROMS (Regional Oceanic Modeling System;

139 Shchepetkin and McWilliams 2005) as well. The UBS scheme adds some dissipation in the high-frequency part which reduces

140 noise in the velocity field. The 4th order vertical scheme, on the other hand, is less dissipative and can retain sharp gradients

141 better (e.g. in a stratified two-layer flow). For tracers, we use the 4th order Flux Corrected Transport (FCT) scheme in both

142 horizontal and vertical directions; the vertical scheme uses the COMPACT formulation. The 4th order FCT schemes ensure

143 lower numerical dissipation while being positive definitive, i.e. they do not generate any spurious overshoots in the tracer fields.

144 Switching to these higher-order advection schemes significantly improved the magnitude of salt inflow to the Arkona basin

145 (not shown).

146 Our tests also indicated that the vertical eddy diffusivity from the turbulence model caused excessive vertical mixing in

147 the Belt Sea–Arkona region, effectively stopping the propagation of the inflows. As a remedy, we lowered the Galperin limit

148 parameter in the $k - \varepsilon$ model to a value 0.10. In contrast, the value 0.17 was used in Nemo-Nordic 1.0 (Hordoir et al., 2019).

149 ## 2.3 Boundary conditions and forcings

150 The simulation covers a 2-year period from October 1, 2014 to September 30, 2016. Initial conditions for water temperature

151 and salinity were obtained from a spin-up run (see below). SSH and velocity were initialized as zero. Because the model is

152 initialized at rest, the first month of the simulation is excluded from the analysis and the model assessment is carried out for

153 the remaining 23 months (November 1, 2014 to September 30, 2016).

154 The model is forced with the 3 km HIRLAM atmospheric forecast model data (http://hirlam.org, last access: March 29,

155 2021). The 10 m wind, 2 m air temperature, 2 m specific humidity, incoming long and short wave radiation, total precipitation,

156 solid precipitation, and surface atmospheric pressure fields at 1 h temporal resolution are fed to the NEMO model. We use

157 the NCAR bulk formulae (Large and Yeager, 2004) of the Aerobulk package (Brodeau et al., 2016) to evaluate the turbulent

158 air–sea fluxes. To account for slightly underestimated wind speeds in the atmospheric model, the wind stress was multiplied

159 by a factor 1.1. Atmospheric pressure gradient is applied in the momentum equation.

Along the open boundaries in the North Sea, SSH, depth-averaged velocity, as well as vertical profiles of temperature and salinity are prescribed from the CMEMS Northwestern Shelf forecast model (Graham et al., 2018). The Flather scheme (Flather, 1994) is used for the barotropic mode while the Flow Relaxation Scheme (Davies, 1976) is used for the tracers. This configuration is sufficient to prescribe the tidal signal in the North Sea, and sub-tidal variation of SSH, temperature and salinity.

The spin-up run (April 1, 2011 – September 30, 2014) was initialized with temperature and salinity from climatology and forced with earlier HIRLAM atmospheric data, and SMHI NEMO storm surge model data at the open boundary. For the last month (September 2014), the open boundary conditions were identical to the final simulation.

River forcing data were obtained from the EHYPE model (Arheimer et al., 2012). River discharge and water temperature are prescribed at 729 rivers along the coasts with 1 day temporal resolution. Salinity of riverine water is set to zero.

2.4 Observations

Observational data were obtained from the Copernicus Marine Environment Monitoring Service (CMEMS) near-realtime, in-situ observation catalog (`INSITU_BAL_NRT_OBSERVATIONS_013_032`). SSH data was obtained from 45 tide gauges across the whole Baltic basin (red markers in Fig. 1). In addition, four tide gauges in the North Sea were included (from product `INSITU_NWS_NRT_OBSERVATIONS_013_036`; Fig. 1 a). Tide gauge sea surface temperature (SST) observations were scarcer, focused more on the southern part of the basin (black markers). The temporal resolution of the tide gauge data was either 10 min, 15 min, or 1 h.

Vertical profile data of water temperature and salinity were obtained at locations shown with yellow markers. Only stations with more than 6 profiles in the study period were included in the analysis. In addition, continuous vertical profile observations from the Arkona buoy (indicated by a yellow square in Fig. 1) were used; The data contain temperature and salinity observations at 1 h temporal resolution from eight CTDs at different depths (2 to 43 m).

FerryBox surface temperature and salinity observations were included from two ferries, TransPaper, and FinnMaid (routes are shown in Figure 1 b.). The two FerryBoxes take measurements at 3 and 5 m depth, respectively. As the observations have high sampling rate (typically < 30 s), the data was binned to 10 min temporal resolution. The binned data consists of mean temperature, salinity, and ship location during the 10 min time window. Furthermore, the data was manually quality checked to remove spurious values (such as abnormally long periods showing constant salinity or temperature).

The salinity observations are in practical salinity units; for model assessment, the observed salinity was converted to Absolute Salinity units. Prior to computing the error metrics, the model data was interpolated to the observation locations and time stamps. Unless otherwise specified, spatial interpolation was carried out with nearest neighbor search while linear interpolation was used in time.

Sea ice extent was computed from digitized ice charts by the Finnish Meteorological Institute. The ice chart frequency varied between 1 and 7 days in the study period. In the beginning of the ice season when ice coverage is scarce, ice charts are usually generated at 3 or 4 day intervals. Daily charts are typically available from late December onward.

2.5 Model assessment metrics

The model skill is quantified with standard statistical measures. Let o_i and m_i, $i = 1, \ldots, N$ be the observed and modeled time series, respectively. Denoting the mean of the time series by $\overline{m}$, the bias, Root Mean Square Deviation (RMSD) and Centered Root Mean Square Deviation (CRMSD) are defined as

$$\mathrm{BIAS} = \overline{m} - \bar{o},$$

$$\mathrm{RMSD}^2 = \frac{1}{N} \sum_{i=1}^{N} (m_i - o_i)^2,$$

$$\mathrm{CRMSD}^2 = \frac{1}{N} \sum_{i=1}^{N} \left((m_i - \overline{m}) - (o_i - \bar{o}) \right)^2.$$

Standard deviation (σ_m) and correlation coefficient (R) are given by

$$\sigma_m^2 = \frac{1}{N} \sum_{i=1}^{N} (m_i - \overline{m})^2,$$

$$R = \frac{1}{\sigma_o \sigma_m} \frac{1}{N} \sum_{i=1}^{N} (m_i - \overline{m})(o_i - \bar{o}).$$

CRMSD is related to σ_m and R through the equation,

$$\mathrm{CRMSD}^2 = \sigma_o^2 + \sigma_m^2 - \sigma_o \sigma_m R, \tag{2}$$

which can be visualized in a Taylor diagram (Taylor, 2001). In this work, we are normalizing the Taylor diagram by scaling the variables with σ_o:

$$\mathrm{NCRMSD}^2 = 1 + \sigma_m'^2 - \sigma_m R, \tag{3}$$

$$\mathrm{NCRMSD} = \frac{1}{\sigma_o} \mathrm{CRMSD},$$

$$\sigma_m' = \frac{\sigma_m}{\sigma_o},$$

where NCRMSD and σ_m' are the normalized CRMSD and standard deviation of the model, respectively. Normalization leads into dimensionless metrics and permit comparison of different data sets in a single figure. As the Taylor diagram does not contain the bias, SST comparisons also include a target diagram depicting normalised bias, $\mathrm{NBIAS} = \mathrm{BIAS}/\sigma_o$, and NCRMSD. In the target diagram, NCRMSD has been augmented with the sign of $\sigma_m - \sigma_o$. We also use normalized RMSD, $\mathrm{NRMSD} = \mathrm{RMSD}/\sigma_o$. NRMSD is a useful dimensionless metric: The value 1.0 can generally be regarded as a threshold for poor model skill. Indeed, setting m_i to the mean value of the observations results in NRMSD=1.0.

The exact vertical reference datum of the circulation model is not well defined. Consequently, SSH bias cannot be reliably evaluated and we therefore assess SSH performance with centralized metrics, i.e. CRMSD and Taylor diagrams.
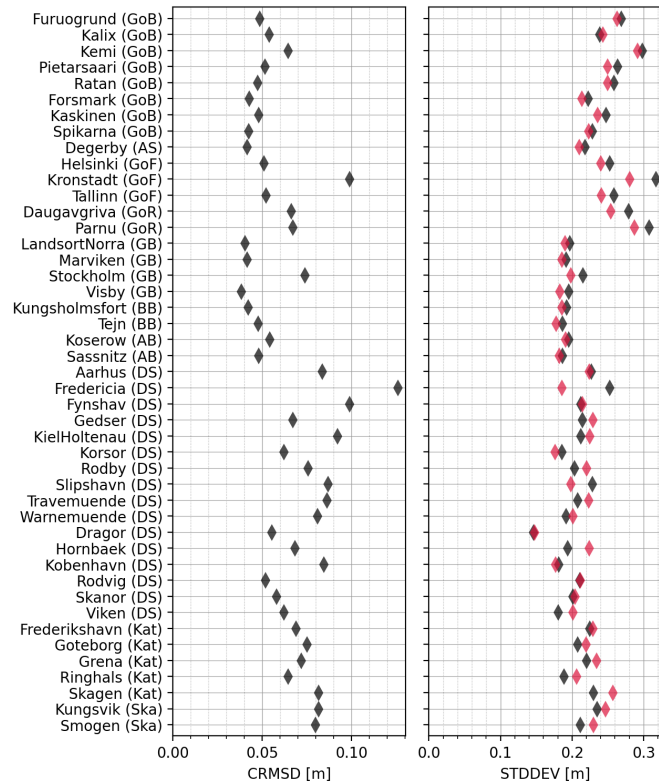
Figure 2. Sea surface height error metrics. Black and red symbols denote the model and observations, respectively. See Figure 1 for station locations. Sub-basins are indicated by the abbreviations: GoB, Gulf of Bothnia; AS, Archipelago Sea; GoF, Gulf of Finland; GB, Gotland Basin; BB, Bornholm Basin; AB, Arkona Basin; DS, Danish Straits; Kat, Kattegat; Ska, Skagerrak.

3 Results

3.1 Sea surface height

SSH error metrics (CRMSD and standard deviation) are shown in Fig. 2. The model skill is generally good, CRMSD being below 10 cm at most stations. For the Baltic basin (Gulf of Bothnia, Gulf of Finland, Archipelago Sea, Gotland, Bornholm and Arkona basins), CRMSD is below 8 cm indicating that seiche waves are well reproduced. The only exception is Kronstadt, located at the eastern end of Gulf of Finland, where CRMSD is 10 cm. The deviation is generally larger in the Danish Straits and Kattegat/Skagerrak region where tidal variations are significant. The largest errors occur at Fredericia, in the Little Belt region, where CRMSD exceeds 12 cm. The model skill in these locations is affected by the Little Belt topography which is difficult to resolve at 1.8 km resolution; the strait itself is less than 1 km wide in the narrowest part. The model resolution also affects the skill in other locations such as Kobenhavn in the Sound, and stations along the German coast of the Belt Sea
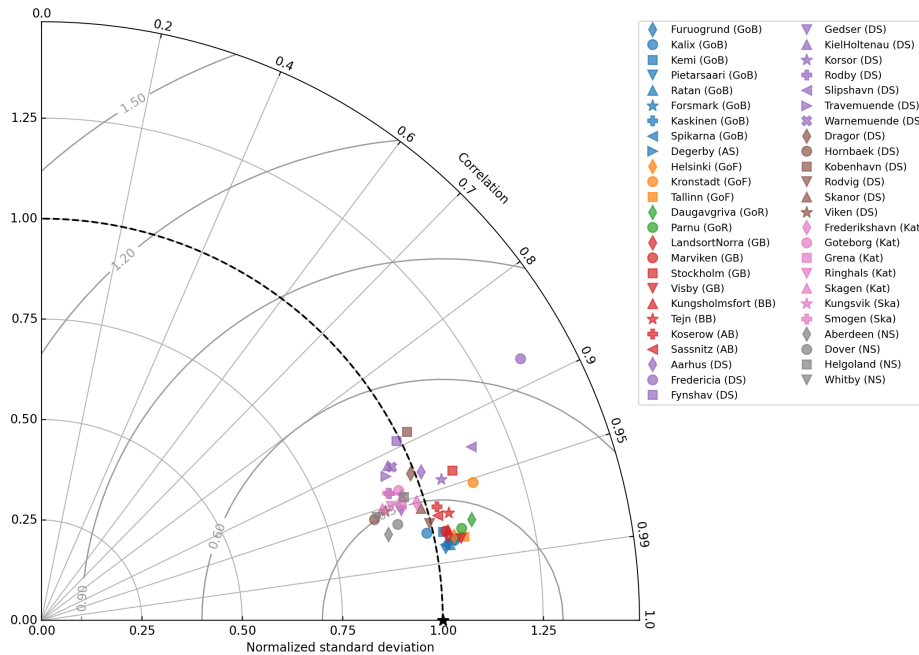
Figure 3. Taylor diagram of sea surface height error metrics. The metrics have been normalized by the standard deviation of the observations. See Figure 1 for station locations; The sub-basin abbreviations are as in Fig. 2; NS stands for the North-Sea.

227 (KielHoltenau, Warnemuende, Travemuende). All of these tide gauges are located inside an estuary mouth or harbor area which

228 the present model cannot resolve.

229   In general, the model reproduces SSH standard deviation well (Fig. 2). The difference is within 2 cm in most cases; the

230 largest deviation at Fredericia is approximately 7 cm. In the Baltic basin, the model has a tendency to overestimate variability.

231 In the Danish Straits, the variability is slightly underestimated at several locations although overestimation also occurs.

232   The Taylor diagram (Fig. 3) shows that the model reproduces SSH variability well. Most stations have NCRMSD < 0.45,

233 and the correlation coefficient is generally above 0.90. The agreement between model and the SSH observations is generally

234 higher in the open Baltic Sea than in Danish Straits. In the Baltic Sea, the NCRMSD is below 0.3 (except at Kronstadt and

235 Stockholm) and the correlation coefficient is above 0.95 (except at Stockholm). In the Danish Straits, stations Fredericia,

236 Kobenhavn, and Fynshav show much lower correlations below 0.9. This local drop in the performance is expected due to the

237 complex bathymetry in the Danish Straits. Similarly, the lower performance at Stockholm is likely affected by the archipelago

238 which is not fully resolved in the model.

239   Figure 3 includes four tide gauges in the North Sea (gray symbols) where the tidal range is much larger. The tides are

240 well reproduced ($R > 0.94$). Performance is the best at Aberdeen and Dover; At Helgoland, the performance is similar to

241 Kattegat/Skagerrak stations. Standard deviation is slightly underestimated.
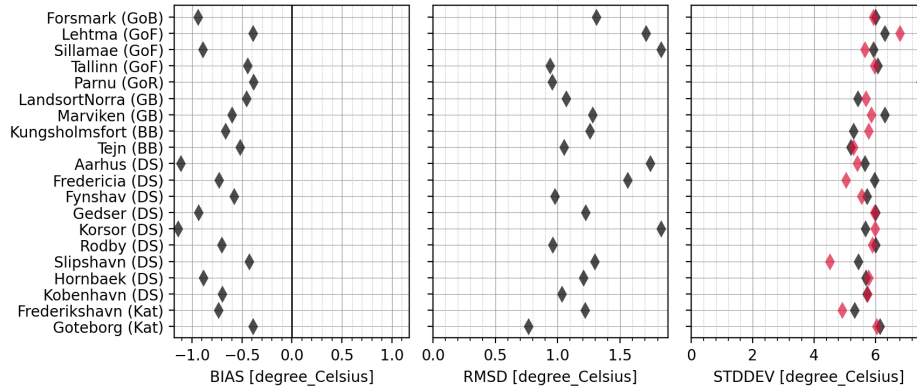
Figure 4. Surface temperature error metrics. Black and red symbols denote the model and observations, respectively. See Figure 1 for station locations; The sub-basin abbreviations are as in Fig. 2.
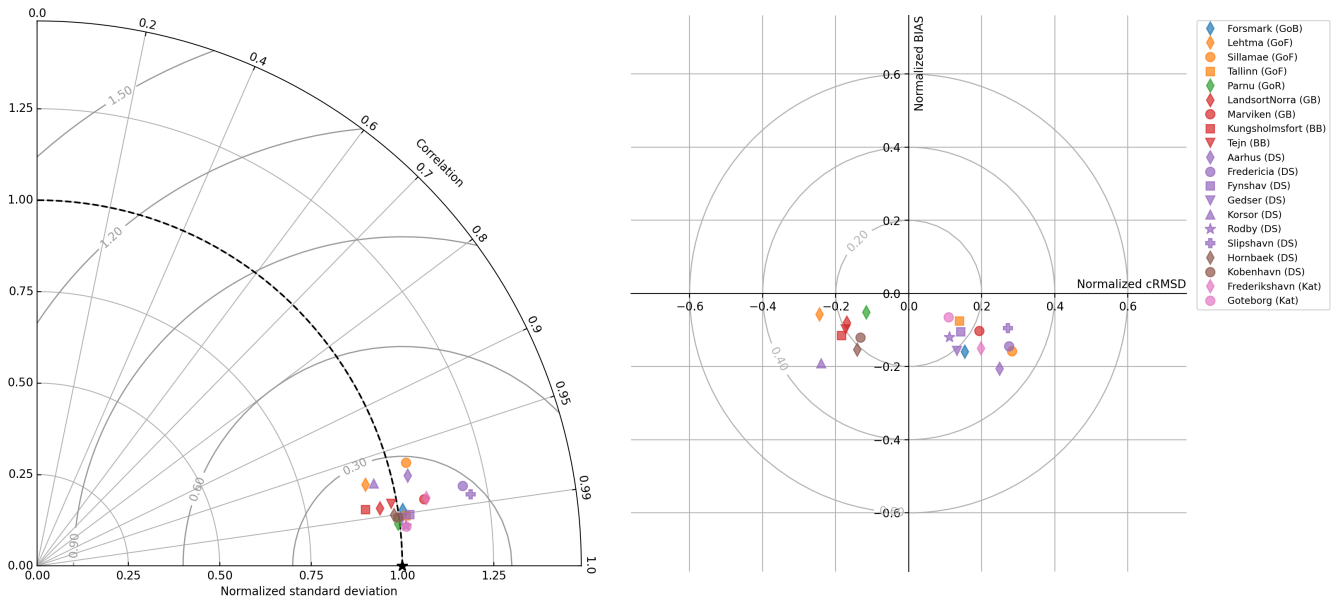
Figure 5. Taylor and target diagram of surface temperature error metrics. The metrics have been normalized by the standard deviation of the observations. See Figure 1 for station locations; The sub-basin abbreviations are as in Fig. 2.

3.2 Sea Surface Temperature and Salinity

Sea surface temperature (SST) is mostly governed by surface heat fluxes, driven by the seasonal cycle of solar radiation and air temperature, and vertical mixing in the water column. In addition, near the coast (where tide gauges are located), riverine heat flux can cause local variations.
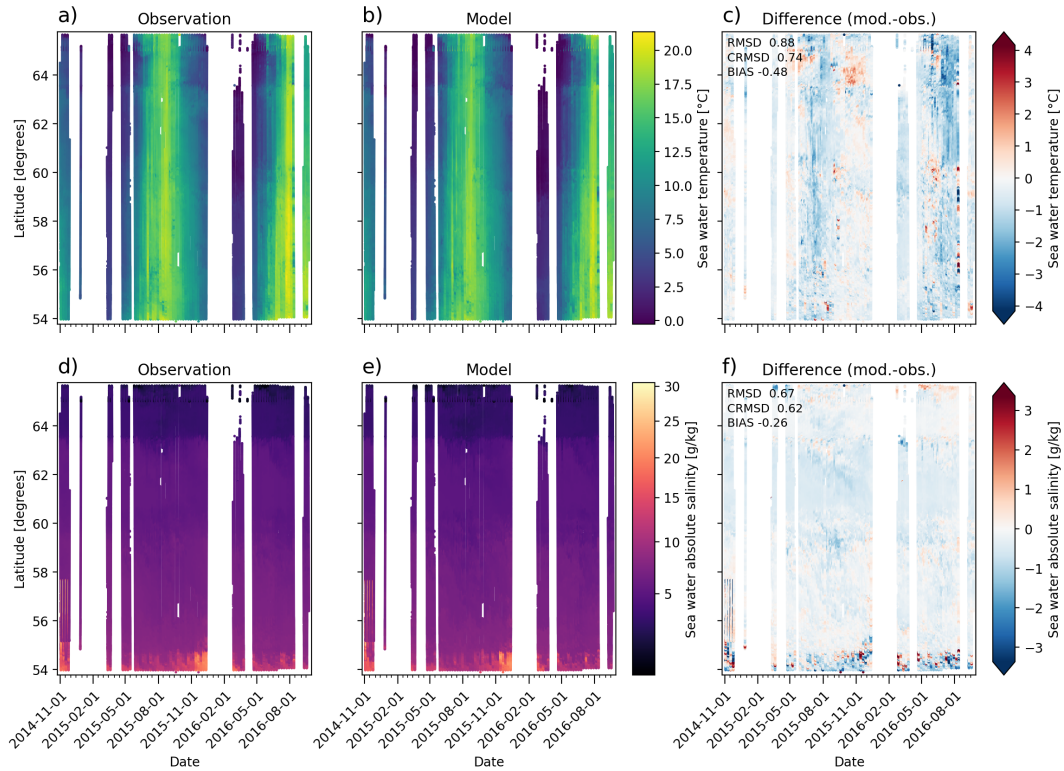
Figure 6. Surface temperature and salinity comparison against TransPaper FerryBox observations. The ferry operates between Oulu (top) and Lübeck (bottom; route is shown in Fig. 1 b). In the beginning of the data set (November 2014) the ferry also visited Gothenburg.

246   Tide gauge SST metrics are shown in Fig. 4. In general, there is no clear pattern across the domain. The model has a
247   negative bias (typically between –0.4 and –0.9°C) at almost all stations; the largest bias (exceeding –1.1°C) occurs at Korsor.
248   The RMSD is below 1.9°C in all cases. The standard deviation is typically close to the observed value.

249   The Taylor diagram (Fig. 5, left) shows that SST skill is good in general. All locations are within 0.30 NCRMSD, and have
250   a correlation coefficient above 0.95. The normalized standard deviation is generally close to unity except at Fredericia and
251   Slipshavn. The metrics indicate that the model captures the seasonal SST variability well. The normalized target diagram (Fig.
252   5, right) shows that the negative bias is quite small (typically NBIAS < 0.20) compared to the overall SST variability (i.e.
253   seasonal cycle).

254   Comparison against FerryBox SST from the TransPaper and FinnMaid ferries are shown in Figures 6 and 7, respectively (top
255   row). Although the FerryBox data has sparser temporal coverage than the tide gauge observations, it is useful for validating
256   the modeled SST in open waters away from the coasts. Also here the annual temperature cycle is well reproduced. The model
257   bias is less than –0.5°C for the two ferries (Fig. 6c and 7c). RMSD is below 0.9°C, suggesting that SST performance is better
258   in the open sea than at the tide gauge locations.
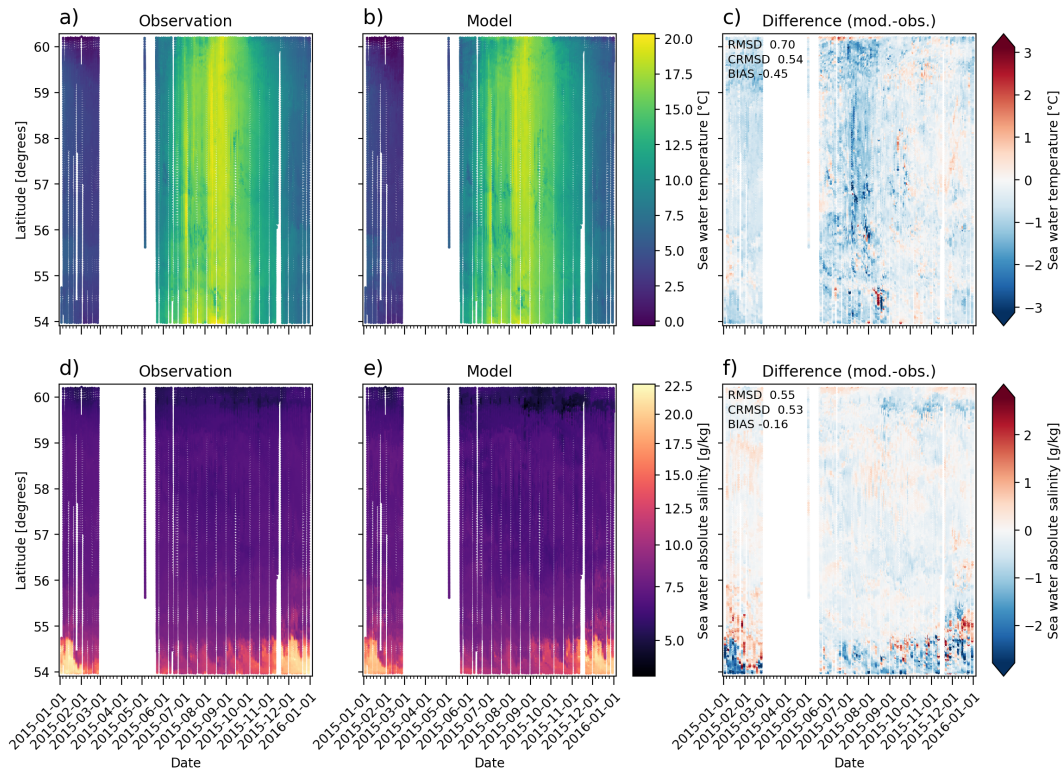
Figure 7. Surface temperature and salinity comparison against FinnMaid FerryBox observations. The ferry operates between Helsinki (top) and Lübeck (bottom; route is shown in Fig. 1 b).

259   The TransPaper comparison shows a negative bias in the Baltic Proper and Gulf of Bothnia in summer 2015 (June–July; Fig.
260   6 c). The bias is smaller during the following fall (October–December). A negative bias is visible in summer 2016 as well. The
261   shorter FinnMaid data set also shows the negative bias during summer 2015 (Fig. 7 c). Although the data coverage is sparse,
262   the comparison therefore suggest that the model has a negative bias during summer months (June–July) whereas the bias is
263   smaller in fall. The magnitude of these deviations is, however, typically below 1.5°C.

264   FerryBox Sea surface salinity (SSS) comparison is shown in Figures 6 and 7 (bottom row). TransPaper observations (Fig.
265   6d) clearly show the SSS gradient ranging from roughly 15 g/kg in the Belt Sea to 0 g/kg in the northern part of the Bothnian
266   Bay. In November 2014, the ferry also visited Gothenburg where SSS can reach 30 g/kg. The model reproduces the horizontal
267   salinity gradient well, bias is -0.26 g/kg and RMSD is 0.67 g/kg; In the FinnMaid data set (Fig. 7f), the bias and RMSD are
268   similar, -0.16 and 0.55 g/kg, respectively. In both cases, the deviation is the largest in the Belt Sea and Kattegat where the model
269   predominantly underestimates SSS. The larger error magnitude is due to the significant salinity gradients and their temporal
270   variability in this region. The model has a small negative bias (-1 g/kg) in the Bothnian Sea (Fig. 6f). A negative bias is seen in
271   the Gulf of Finland as well (around latitude 60°N; Fig. 7f).
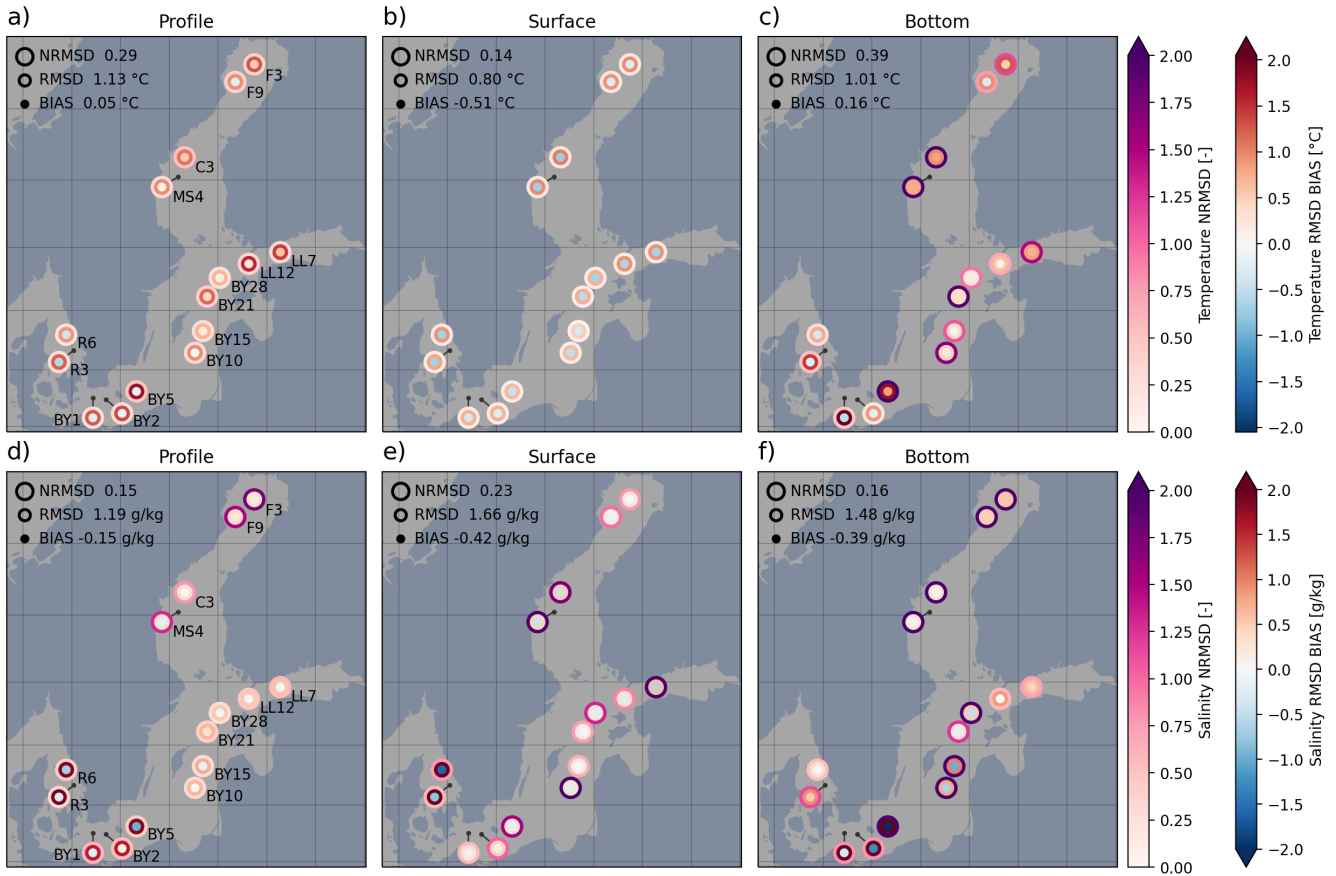
Figure 8. Vertical profile comparison against vessel observations; Temperature (top row) and salinity (bottom row). The dots depict NRMSD (outer ring), RMSD (inner ring), and BIAS (center dot). The metrics have been calculated for the entire profile (a,d), surface 10 m (b, e) and bottom (c, f). Combined metrics over all the stations is printed in each panel. Bottom values were computed for the lowest 15% of the water column.

3.3 Vertical profiles

Figure 8 shows comparison of temperature and salinity profiles against research vessel observations. In all panels, the outer ring denotes NRMSD, the middle ring RMSD, and the center dot the BIAS. RMSD and BIAS are visualized using the same color map; in all cases light color indicates small deviation. In addition, the metrics across all the plotted stations are printed in the upper left corner.

The temperature profile metrics (Fig. 8a) are quite similar throughout the Baltic Sea. NRMSD is below 0.5 at all locations (except at C3 where NRMSD is 0.54) indicating good skill. The metrics for surface temperature (top 10 m; Fig. 8b) show low deviations. The NRMSD of the combined data set is 0.14 and bias is -0.51°C. The high surface temperature skill is consistent

with SST results presented in Sect. 3.2: the model can capture the seasonal surface temperature variability driven by the solar radiation. Based on the SST and profile metrics, the model reproduces surface layer temperature well.

The bottom temperature skill is poorer (Fig. 8c). RMSD in the Gotland basin is quite low (below 0.5°C) while being higher in the Gulf of Finland and Gulf of Bothnia (0.6 to 1.3°C). In these regions, however, NRMSD exceeds value 2.0 at several stations: While RMSD is moderate, the deviation is significant compared to the low variability of bottom temperature. The bias tends to be positive in the Baltic basin, and negative in Kattegat and the Arkona basin. The largest deviation occurs at BY1 where RMSD reaches 2.0°C.

The model reproduces salinity profiles relatively well (Fig. 8d). The deviation is small (RMSD < 0.73 g/kg) in the Gotland basin and Gulf of Finland. NRMSD is large in the Gulf of Bothnia due to the fact that salinity is low in this region as a result of riverine freshwater input. In contrast, in the Danish Straits and Kattegat NRMSD is small while RMSD is relatively high (up to 1.9 g/kg) due to the opposite reason: In this region, salinity regularly varies by more than 10 g/kg.

Surface salinity metrics (Fig. 8e) are generally similar to the whole profile metrics, except NRMSD is high in the Bothnian Sea, Gulf of Finland, and southern Gotland basin.

The bottom salinity metrics are presented in Fig. 8f. NRMSD regularly exceeds 2.0 in the Baltic basin because the variability of bottom salinity is small. A significant negative bias is visible in the Arkona and especially Bornholm basin; the bias is negative also in the Gotland basin. The deviation is moderate in Kattegat and the Gulf of Finland. While absolute deviation is small in the Gulf of Bothnia, NRMSD is large. In general, the results indicate that bottom salinity is underestimated in the Arkona, Bornholm, and Gotland basins. The skill is poorest in Bornholm (BY5). At this location, the model reproduces the halocline correctly but tends to underestimate bottom salinity. During the first simulated year the deviation is roughly –2 g/kg; after November 2015 it is –4 g/kg.

3.4   The 2014 Major Baltic Inflow event

A Major Baltic Inflow (MBI) event occurred in December, 2014. Mohrholz et al. (2015) divided the event into four phases: During the outflow period (November 7 – December 3 2014) strong easterly winds pushed surface waters from the Baltic Sea to Kattegat, lowering the mean sea level at Landsort by 57 cm. After the winds ceased for a couple of days, the inflow period was characterized by strong westerly winds. The precursory period (December 3 – December 13, 2014) brought saline waters through the Sound and into the Belt Sea. On December 13, the saline inflow had reached Darss Sill. At the buoy, the salinity exceeded 17 g/kg in the entire water column, marking the beginning of the main inflow period. The main inflow period lasted until December 25, 2014, when the westerly winds, and hence the barotropic inflow, ceased. During this time, the mean sea level at Landsort rose 95 cm from the lowest value, until the dense saline water mass had reached the Arkona basin. In the post-inflow period (starting on December 25, 2014), the saline water mass crept further into the Bornholm basin, and the following downstream sub-basins, driven by the baroclinic pressure gradient (density difference).

The observed salinity from the Arkona Buoy is shown in Figure 9 (panel a). The main salt pulse arrives at the buoy on December 16, 2014. On December 20, 2014, the dense water reaches 16 m depth. The model replicates the arrival of the pulse on December 16, 2014 and the main inflow phase (December 20 to December 26, 2014; Figure 9b). The bottom salinity
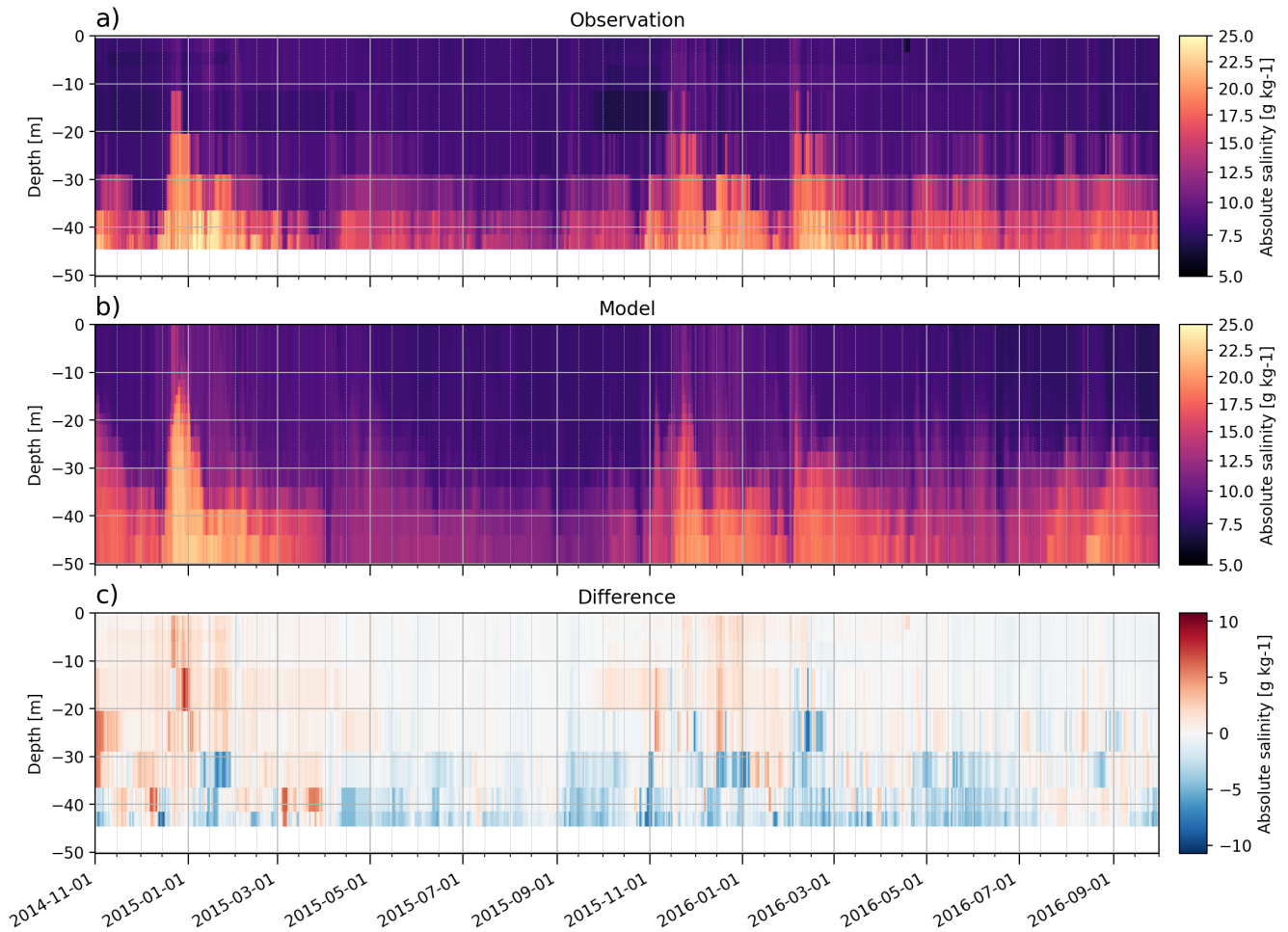
Figure 9. Vertical profile of salinity at Arkona. a) Observations; b) model; c) Difference (model minus observations). The difference field has been computed by interpolating the model data to the observation locations.

314   is underestimated during the onset of the pulse (December 12 to 20 2014) from January 4 2015 onward (Figure 9c). Most

315   notably, the observations show a secondary salt pulse in April 2015 which is underestimated in the model. The subsequent

316   stronger pulses, in November 2015 and March 2016, are reproduced but their magnitude are also slightly underestimated. In

317   general, the model captures the MBIs but has a tendency to underestimate salinity at the bottom, and overestimate it in the rest

318   of the water column (up to 35 m depth).

319   A time series of bottom salinity at the Arkona Buoy is shown in Fig. 10 (panel a), accompanied by observations at BY5

320   (Bornholm basin; panel b), BY10 (Gotland basin; panel c), and BY15 (Gotland deep; panel d). As stated above, the inflow

321   reaches Arkona on December 16. First observation of elevated salinity at BY5 is from February 19 2015 but due to the gap in

322   the measurements the pulse may have arrived earlier. At BY10 and BY15, an elevated bottom salinity is observed on February
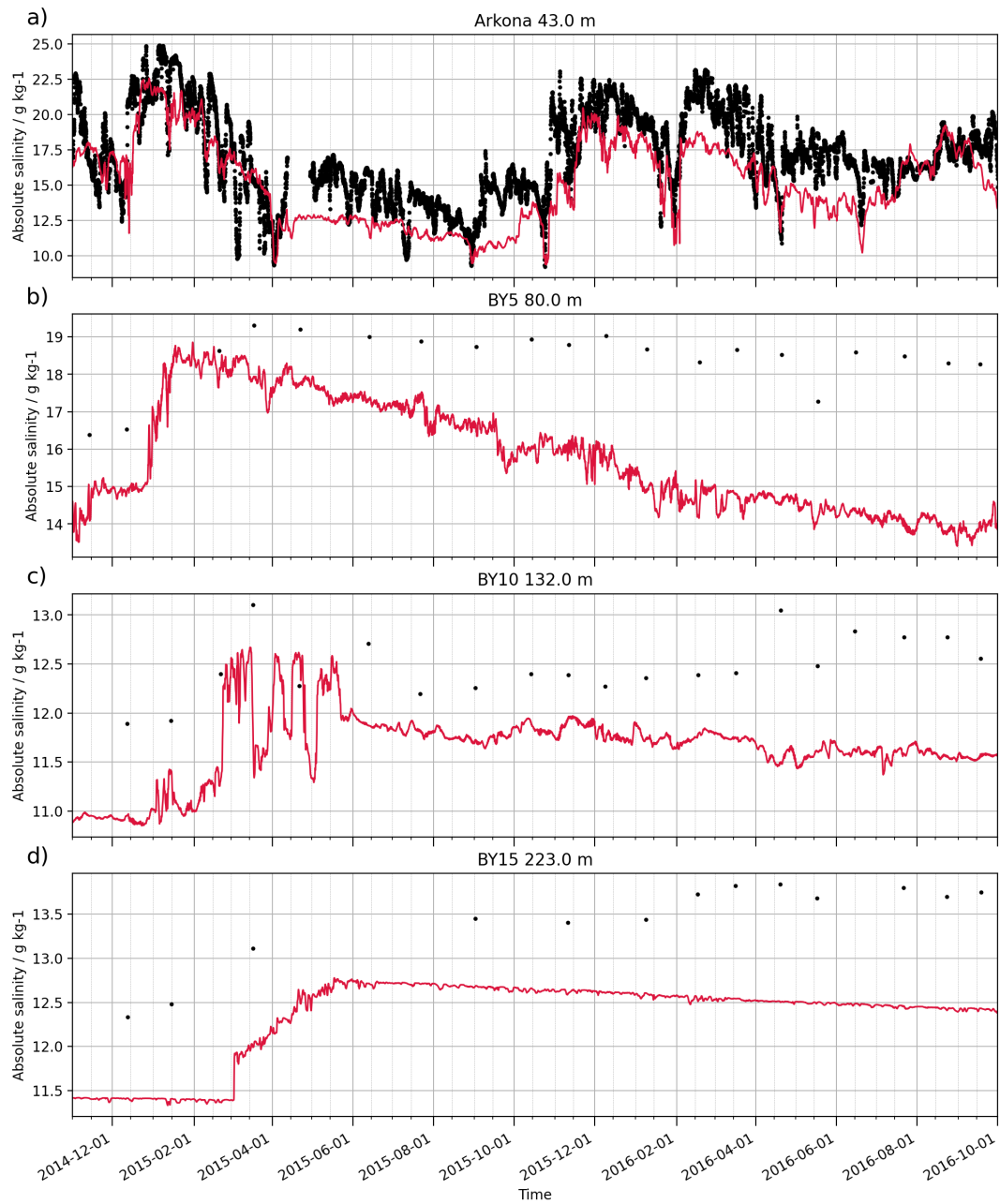
Figure 10. Time series of bottom salinity at selected locations. The red line denotes the model, the black dots are the observations.

21 and March 17, respectively. The timing is quite well captured by the model: At Arkona the salt pulse is delayed by 1.5 days. The modeled salt pulse reaches BY5 at the end of December 2014, BY10 in the end of February 2015 and BY15 in the beginning of March 2015. The model underestimates the maximum bottom salinity by roughly 2.5 g/kg at Arkona, 0.5 g/kg
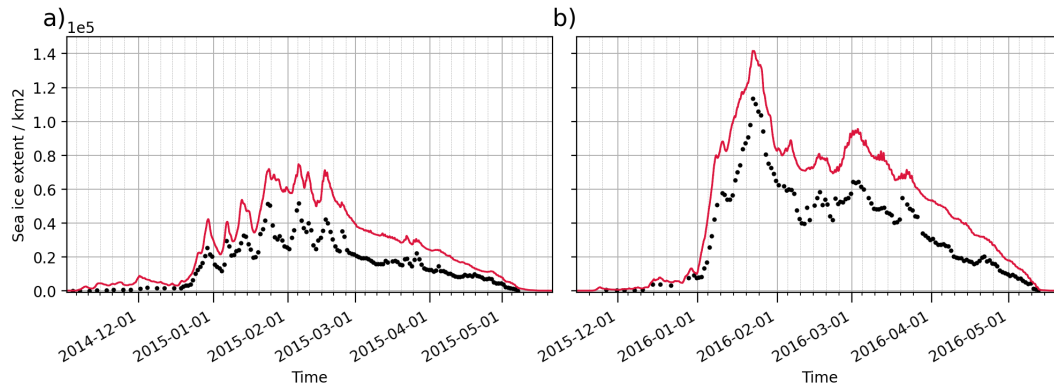
Figure 11. Time series of sea ice extent in the Baltic Sea for the two simulated winters. The red line denotes the model, the black dots are the observations.

326 at BY5, 0.3 g/kg at BY10. The deviation, however, increases in time at BY5, BY10 and BY15. At BY5, the observed salinity
327 remains above 18 g/kg (most of the time) after March 2015 while the modeled salinity decreases over time; in September 2016
328 the model underestimates salinity by 4 g/kg.

329 A similar decrease in modeled salinity, although smaller in magnitude, is also seen at BY10 and BY15. The observations
330 show a subsequent increase of bottom salinity (in February and April 2016 at BY15 and BY10, respectively) but the model
331 does not capture these events. In summary, the results indicate that the model does reproduce magnitude and timings of the
332 2014 MBI event and its propagation into the Baltic Proper. It does, however, underestimate the bottom salinity by 1 to 4 g/kg,
333 and does not reproduce lesser MBI events observed in 2015 and 2016. The negative salinity bias is also seen in the profile
334 statistics (Figure 8f).

3.5 Sea Ice

336 Sea ice extent (defined as the total area where the sea ice area fraction exceeds 0.15) is presented in Fig. 11 for the winters
337 2014/2015 (panel a) and 2015/2016 (b). The winter 2014/2015 was exceptionally mild with only about 50 000 km^2 sea ice
338 extent whereas the winter 2015/2016 was quite typical; maximum ice extent, 120 000 km^2, was observed in January 2016.
339 During both winters, the model tended to overestimate the ice extent by roughly 25 000 km^2. In relative numbers, the maximum
340 ice extent was overestimated by 45% and 25% for the two winters, respectively. The ice season also started earlier in the model,
341 especially in November 2014.

342 The spatial distribution of modeled sea ice is compared against FMI ice charts in Figure 12. The shown dates correspond to
343 the largest sea ice extent in the ice charts for winters 2014/2015 and 2015/2016. In both cases, sea ice is formed in the Bothnian
344 Bay and eastern part of the Gulf of Finland. In the colder winter 2015/2016, ice coverage extends to the northern part of the
345 Bothian Sea, the Archipelago Sea and the northern part of the Gulf of Riga. Generally, the modeled ice coverage agrees well
346 with the ice charts. Most notable difference is the open water area in the Bothnian Bay (Fig. 12b,d) which the model does not
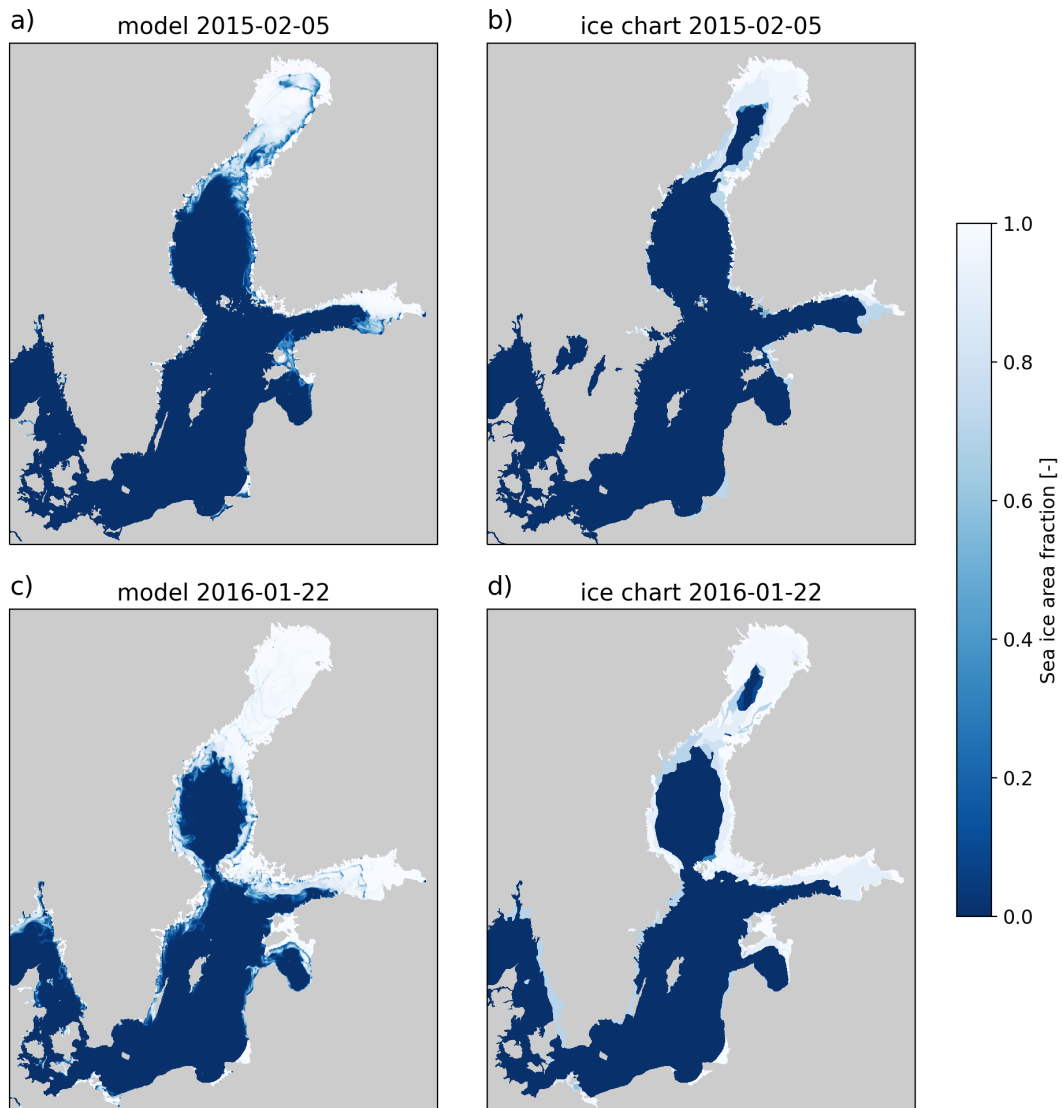
Figure 12. Comparison of sea ice area fraction from the model (a,c) and ice charts (b, d) for the maximal sea ice extent conditions in 2015 and 2016.

reproduce. The model has a tendency to form more ice near the coasts (e.g. along the coast of Sweden). The model field also shows larger areas with low (<0.4) sea ice area fraction, which may contribute to the larger extent seen in Figure 11.

3.6   SSH under storm conditions

To assess how well the model is able to reproduce sea level variations under storm conditions, we analyze the Elon and Felix storms that occurred between January 7 and 12, 2015 (Fig. 13). The storms created strong westerly winds in the southern
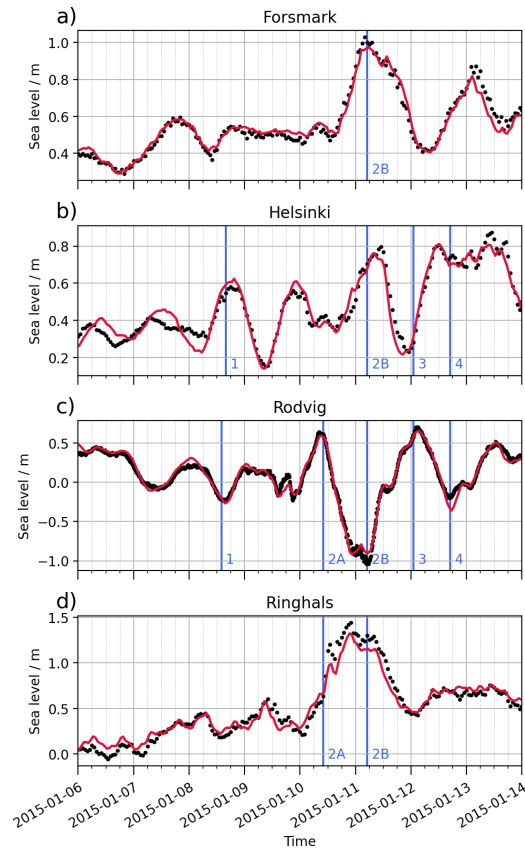
Figure 13. Time series of sea levels at selected locations during Elon and Felix storms. The red line denotes the model, the black dots are the observations. The blue vertical lines indicate events discussed in the text. The model data has been bias corrected for visual comparison.

352 Baltic, with daily mean wind speed between 10 and 18 m s^{-1}. Figure 13 shows SSH time series at four stations in different
353 parts of the Baltic Sea to illustrate the propagation of seiche oscillations.

354   On January 8, westerly winds pushed water from the southern Baltic Sea to the east, lowering sea level in the Arkona basin
355 and increasing it in the Gulf of Finland (event 1 in Fig. 13b,c); as the winds calmed, sea level at Helsinki retracted. The main
356 storm event occurred on January 10, when strong westerly winds pushed water from the North Sea to Kattegat (Fig. 13d).
357 Initially, sea levels rose in the Arkona basin (event 2A in Fig. 13c) but as winds prevailed and moved to the east, sea levels
358 dropped by roughly 1.5 m in 12 h (2B). This led to a sea level increase in the Gulf of Finland and the Bothnian Sea (2B in Fig.
359 13a,b). On January 11, northerly winds pushed water to the south, causing an opposite sea level change (event 3). This was
360 followed by another weaker westerly wind event (event 4).

361   Overall the model captured the wind-driven water elevation variations in the southern Baltic Sea. The extremes are slightly
362 underestimated: the maximum observed and simulated SSH range at Rodvig are 1.68 and 1.55 m, respectively. At Ringhals the
363 values are 1.40 and 1.27 m. The modeled seiche oscillations in Gulf of Bothnia and Gulf of Finland (Fig. 13a,b) are in good

364 agreement with the observations. In Helsinki, the amplitude tends to be slightly overestimated and there is a phase lag of 1 to
365 2 h. The tendency to underestimate SSH variability in the Danish Straits region, and overestimate it in the Baltic basin agrees
366 well with the results of long-term validation using tide gauge data (Fig. 3).
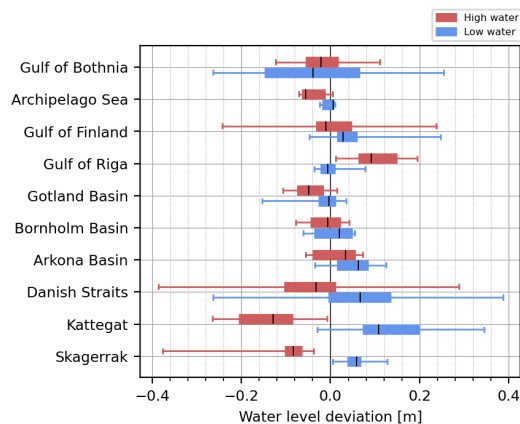
Figure 14. Model deviation in extreme water level cases in different sub-basins. Red and blue bars indicate model's deviation from the observed SSH maximum and minimum, respectively. Positive values mean that the modeled SSH is higher. The thin line denotes the entire deviation range; thick bars indicate the 25 to 75 percentile range. Black line denotes the mean. The sub-basins are defined as in Fig. 2.

367   To assess how well the model captures high and low SSH events during the entire simulation period, we identified five
368 highest and five lowest SSH extremes in each tide gauge time series. The corresponding maximum/minimum SSH levels
369 were identified from the model within a 6 h window from the observation extremum. Model's deviation from the observed
370 peak/through was then calculated. Prior to the analysis, mean SSH was removed from both the observation and model data.
371 The results are summarized in Fig. 14.
372   The model tends to underestimate high SSH values especially in the tidally dominated regions (Danish Straits, Kattegat, and
373 Skagerrak). Low SSH values are similarly underestimated (i.e. positive deviation) in these regions. In general, the spread of the
374 deviation is larger (up to 70 cm) in the tidally dominated regions while being small in the deeper basins (within 20 cm). The
375 spread is larger in the Gulf of Bothia and Gulf of Finland due to SSH build up in these elongated basins. High SSH events are
376 overestimated in the Gulf of Riga. These results confirm that the model tends to underestimate SSH variability in the Danish
377 waters while it is slightly overestimated in the Gulf of Bothia and Gulf of Finland.

4   Discussion and conclusions

379 The presented skill assessment for the 23 month period (November 1, 2014 – September 30, 2016) shows that the model
380 captures the main hydrographic features of the Baltic Sea. SSH variability is well reproduced. SSH skill is especially good in
381 the Baltic basin: CRMSD is typically below 7 cm. In the Danish Straits region, the deviation is larger due to the interaction of
382 the tides and the complex topography. The SSH metrics indicate that the tides propagate from the North Sea to Skagerrak and

383 Kattegat without much loss of accuracy. SSH performance drops in the Danish Straits region, most likely due to insufficient

384 horizontal resolution. It is worth noting that many tide gauges are located in harbors, river mouth regions, or small embayments

385 which cannot be properly resolved at the used resolution. Under storm conditions, the model reproduces SSH dynamics well

386 but has a tendency to underestimate the extremes. This is attributable to the atmospheric forcing data which generally tends

387 to underestimate extremes during storm events, as well as to the model's dissipation (e.g., caused by coarse grid resolution, or

388 friction parameterization).

389 The SST and SSS are generally well reproduced. In the FerryBox comparison, RMSD values were 0.9°C and 0.70 g/kg,

390 respectively. SST, however, shows a systematic negative bias of approximately -0.5°C. Our calibration runs suggest that the

391 negative SST bias can be related to underestimated vertical mixing. Another possible cause is river runoff temperature which

392 has a strong impact on SST in the vicinity of the river mouth. Yet another possibility is the downward longwave radiation

393 forcing from the atmospheric model. Near the bottom, the temperature deviation is larger and RMSD can exceed 2°C. It

394 should be noted, however, that due to the long residence time of the Baltic Sea (Döös and Engqvist, 2007), the bottom salinity

395 and temperature in the presented simulation does depend on the initial conditions as well.

396 The modeled sea ice coverage is in good agreement with ice charts, but the model tends to overestimate the overall sea ice

397 extent by 25 to 45%. As ice growth is strongly affected by SST, the overestimation is likely affected by the negative SST bias.

398 Our calibration runs indicate that the sea ice model parameters have only a minor effect on the sea ice extent. Further research

399 is needed to improve the biases in SST and sea ice.

400 The model replicates the 2014 MBI event and subsequent inflows in 2015 and 2016. The timing and magnitude of the MBI

401 salt pulse at Arkona compares well with observations and the bottom salinity is only slightly underestimated. In the Bornholm

402 Basin, the MBI is relatively well simulated by the model, especially considering that the initial bottom salinity is slightly

403 low. After the inflow, however, the modelled bottom salinity decreases at a semi-constant rate, and much faster than in reality.

404 There could be several reasons for this. First, the vertical profile comparison (Figs. 9 and 10) suggest too high vertical mixing.

405 It is possible that the vertical resolution is too coarse in the deeper layers (see discussion below), leading to high numerical

406 diffusion. Second, the fast decline in bottom salinity could be due to an absence of smaller inflows after the MBI, which the

407 model is not able to simulate well enough. Third, the type of vertical discretization employed in the model (z^* coordinates) is

408 not so well suited to simulate dense bottom currents over rough topography, which may lead to a spurious vertical circulation

409 (Dietze et al., 2014). Smoothing of the topography between the Arkona Basin and the Bornholm Basin may help in this respect.

410 The volume and propagation of the inflow can also be affected by the horizontal resolution: Inflow through the Sound, for

411 example, is significant, contributing 20 to 30% of the total volume (Mohrholz et al., 2015), yet it is difficult to resolve the

412 narrow strait in operational models (Fischer and Matthäus, 1996; She et al., 2007; Gräwe et al., 2015b).

413 While both the Nemo-Nordic 1.0 and 2.0 versions use 56 vertical levels, their thickness distributions are different. In the 2.0

414 configuration, the surface resolution has been increased from 3 to 1 m in the top 10 m, implying coarser resolution between 50

415 and 200 m depths. Our calibration runs with 75 and 100 vertical levels indicate that higher vertical resolution in 40 to 100 m

416 range improves bottom salinity in the Bornholm basin (not shown). In addition, the strength of the salt inflow is sensitive to the

417 bathymetry in the Danish Straits region (smoothing the bathymetry and deepening the channels), the used advection schemes

418 (UBS for momentum advection), as well as turbulence closure parameters (lowering the Galperin limit). Thus, horizontal and
419 vertical grid resolution, numerical mixing and turbulence parameterizations all play important roles in simulating the inflow
420 dynamics. MBI dynamics will be studied in more detail in the future.

421 From an operational modeling perspective, the presented model configuration delivers sufficient performance, generally
422 comparable to other models (e.g., Meier et al., 1999; Burchard et al., 2009; Dietze et al., 2014; Hordoir et al., 2019). SSH
423 skill is good in the entire Baltic basin. It is worth noting that in short-term forecasts the SSH skill is also highly dependent
424 on the quality of the atmospheric forcing. SST and salinity biases are small or moderate and those can be corrected with
425 data-assimilation. Surface currents are an important product of operational forecasts, used in several applications, such as oil
426 drift modeling. Validating modeled currents, however, is challenging due to the lack of measurements with sufficient spatial
427 and temporal coverage. Comparing simulated currents at 1 nautical mile grid resolution against point measurements poses
428 additional challenges (Lagemaa et al., 2010). Nevertheless, the model's ability to simulate SSH, water temperature and salinity
429 demonstrates that the general circulation and dynamics are captured fairly well even though direct validation of surface currents
430 was not possible.

431 Improving the model skill is an ongoing effort. The bathymetry can be further improved to better represent the coast line
432 and shallow coastal regions, as well as unresolved channels. The wetting and drying capability of NEMO (O'Dea et al., 2020)
433 could improve SSH in shallow regions. Using higher vertical resolution will likely result in improved salt inflow dynamics.
434 Further work is needed to calibrate advection schemes, diffusion parameterizations, and the representations of overflows to
435 reduce numerical mixing. Most notably, adopting high resolution nesting in strategic regions, such as the Danish Straits and
436 the Archipelago Sea could greatly improve the representation of water exchange processes. Finally, data assimilation and online
437 coupling with atmospheric models can be used to further improve the modeling skill.

438 *Code availability.* Nemo-Nordic is based on the NEMO source code version 4.0 (subversion trunk revision 11281), released under the open
439 source CeCill license (https://cecill.info, last access: March 29, 2021). The standard NEMO source code can be downloaded from the NEMO
440 website (http://www.nemo-ocean.eu/, last access: March 29, 2021). The Nemo-Nordic source code used in the present article has been
441 archived on Zenodo (Nemo-Nordic development team, 2021).

442 *Author contributions.* All authors contributed to the conceptualization of the model configuration, parameter tuning and validation. SF, PaL,
443 TK, LA, and IR implemented changes in the model source code, implemented the model configuration and processed forcing data. TK, PaL,
444 SF, LA, IR, IM, AL, SJS, SV contributed to model validation and tuning. TK was responsible for the original draft of the manuscript and
445 data visualization. TK, LA, IR, LT, VH, SF contributed to the review and editing of the manuscript. AN, VH, LT, PrL, and IL contributed to
446 the administration and supervision of the operational model development activities within the CMEMS BAL MFC project.

447 *Competing interests.* The authors declare that they have no conflict of interest.

448 *Acknowledgements.* This work is supported by the Copernicus Marine Environment Monitoring Service (CMEMS). Observational data was
449 provided by DMI, BSH, SHMI, MSI, LEGMA and FMI. This data was collected and made freely available by the Copernicus project and
450 programmes that contribute to it. Data analysis and visualization were carried out with Matplotlib (Hunter, 2007) and Iris (Met Office, 2010
451 - 2020) Python packages. The authors wish to acknowledge CSC – IT Center for Science, Finland, for computational resources.

References

Arheimer, B., Dahné, J., Donnelly, C., Lindström, G., and Strömqvist, J.: Water and nutrient simulations using the HYPE model for Sweden vs. the Baltic Sea basin – influence of input-data quality and scale, Hydrology Research, 43, 315–329, https://doi.org/10.2166/nh.2012.010, https://doi.org/10.2166/nh.2012.010, 2012.

Axell, L.: BSRA-15: A Baltic Sea Reanalysis 1990–2004, Reports Oceanography 45, Swedish Meteorological and Hydrological Institute, SE–601 76 Norrköping, Sweden, 2013.

Berg, P. and Poulsen, J. W.: Implementation details for HBM, Tech. rep., Danish Meteorological Institute, 2012.

Brodeau, L., Barnier, B., Gulev, S. K., and Woods, C.: Climatologically Significant Effects of Some Approximations in the Bulk Parameterizations of Turbulent Air–Sea Fluxes, Journal of Physical Oceanography, 47, 5–28, https://doi.org/10.1175/jpo-d-16-0169.1, https://doi.org/10.1175/jpo-d-16-0169.1, 2016.

Burchard, H., Janssen, F., Bolding, K., Umlauf, L., and Rennau, H.: Model simulations of dense bottom currents in the Western Baltic Sea, Continental Shelf Research, 29, 205–220, https://doi.org/10.1016/j.csr.2007.09.010, https://doi.org/10.1016/j.csr.2007.09.010, 2009.

Daewel, U. and Schrum, C.: Simulating long-term dynamics of the coupled North Sea and Baltic Sea ecosystem with ECOSMO II: Model description and validation, Journal of Marine Systems, 119-120, 30–49, https://doi.org/10.1016/j.jmarsys.2013.03.008, https://doi.org/10.1016/j.jmarsys.2013.03.008, 2013.

Davies, H. C.: A lateral boundary formulation for multi-level prediction models, Quarterly Journal of the Royal Meteorological Society, 102, 405–418, https://doi.org/10.1002/qj.49710243210, https://doi.org/10.1002/qj.49710243210, 1976.

Dietze, H., Löptien, U., and Getzlaff, K.: MOMBA 1.1 – a high-resolution Baltic Sea configuration of GFDL's Modular Ocean Model, Geoscientific Model Development, 7, 1713–1731, https://doi.org/10.5194/gmd-7-1713-2014, https://doi.org/10.5194/gmd-7-1713-2014, 2014.

Döös, K. and Engqvist, A.: Assessment of water exchange between a discharge region and the open sea – A comparison of different methodological concepts, Estuarine, Coastal and Shelf Science, 74, 709–721, https://doi.org/10.1016/j.ecss.2007.05.022, https://doi.org/10.1016/j.ecss.2007.05.022, 2007.

Fischer, H. and Matthäus, W.: The importance of the Drogden Sill in the Sound for major Baltic inflows, Journal of Marine Systems, 9, 137–157, https://doi.org/10.1016/s0924-7963(96)00046-2, https://doi.org/10.1016/s0924-7963(96)00046-2, 1996.

Flather, R. A.: A Storm Surge Prediction Model for the Northern Bay of Bengal with Application to the Cyclone Disaster in April 1991, Journal of Physical Oceanography, 24, 172–190, https://doi.org/10.1175/1520-0485(1994)024<0172:asspmf>2.0.co;2, https://doi.org/10.1175/1520-0485(1994)024<0172:asspmf>2.0.co;2, 1994.

Funkquist, L. and Kleine, E.: HIROMB: An introduction to HIROMB, an operational baroclinic model for the Baltic Sea, Reports Oceanography 37, Swedish Meteorological and Hydrological Institute, SE–601 76 Norrköping, Sweden, 2007.

Graham, J. A., O'Dea, E., Holt, J., Polton, J., Hewitt, H. T., Furner, R., Guihou, K., Brereton, A., Arnold, A., Wakelin, S., Sanchez, J. M. C., and Adame, C. G. M.: AMM15: a new high-resolution NEMO configuration for operational simulation of the European north-west shelf, Geoscientific Model Development, 11, 681–696, https://doi.org/10.5194/gmd-11-681-2018, https://doi.org/10.5194/gmd-11-681-2018, 2018.

Gräwe, U., Holtermann, P., Klingbeil, K., and Burchard, H.: Advantages of vertically adaptive coordinates in numerical models of stratified shelf seas, Ocean Modelling, 92, 56–68, https://doi.org/10.1016/j.ocemod.2015.05.008, https://doi.org/10.1016/j.ocemod.2015.05.008, 2015a.

Gräwe, U., Naumann, M., Mohrholz, V., and Burchard, H.: Anatomizing one of the largest saltwater inflows into the Baltic Sea in December 2014, Journal of Geophysical Research: Oceans, 120, 7676–7697, https://doi.org/10.1002/2015jc011269, https://doi.org/10.1002/2015jc011269, 2015b.

Griffies, S. M. and Hallberg, R. W.: Biharmonic Friction with a Smagorinsky-Like Viscosity for Use in Large-Scale Eddy-Permitting Ocean Models, Monthly Weather Review, 128, 2935–2946, https://doi.org/10.1175/1520-0493(2000)128<2935:bfwasl>2.0.co;2, https://doi.org/10.1175/1520-0493(2000)128<2935:bfwasl>2.0.co;2, 2000.

Gustafsson, B.: Interaction between Baltic Sea and North Sea, Deutsche Hydrographische Zeitschrift, 49, 165–183, https://doi.org/10.1007/bf02764031, https://doi.org/10.1007/bf02764031, 1997.

Gustafsson, B. G. and Andersson, H. C.: Modeling the exchange of the Baltic Sea from the meridional atmospheric pressure difference across the North Sea, Journal of Geophysical Research: Oceans, 106, 19 731–19 744, https://doi.org/10.1029/2000jc000593, https://doi.org/10.1029/2000jc000593, 2001.

Hofmeister, R., Beckers, J.-M., and Burchard, H.: Realistic modelling of the exceptional inflows into the central Baltic Sea in 2003 using terrain-following coordinates, Ocean Modelling, 39, 233–247, https://doi.org/10.1016/j.ocemod.2011.04.007, https://doi.org/10.1016/j.ocemod.2011.04.007, 2011.

Hordoir, R., Axell, L., Höglund, A., Dieterich, C., Fransner, F., Gröger, M., Liu, Y., Pemberton, P., Schimanke, S., Andersson, H., Ljungemyr, P., Nygren, P., Falahat, S., Nord, A., Jönsson, A., Lake, I., Döös, K., Hieronymus, M., Dietze, H., Löptien, U., Kuznetsov, I., Westerlund, A., Tuomi, L., and Haapala, J.: Nemo-Nordic 1.0: a NEMO-based ocean model for the Baltic and North seas – research and operational applications, Geoscientific Model Development, 12, 363–386, https://doi.org/10.5194/gmd-12-363-2019, https://doi.org/10.5194/gmd-12-363-2019, 2019.

Hourdin, F. and Armengaud, A.: The Use of Finite-Volume Methods for Atmospheric Advection of Trace Species. Part I: Test of Various Formulations in a General Circulation Model, Monthly Weather Review, 127, 822–837, https://doi.org/10.1175/1520-0493(1999)127<0822:tuofvm>2.0.co;2, https://doi.org/10.1175/1520-0493(1999)127<0822:tuofvm>2.0.co;2, 1999.

Hunter, J. D.: Matplotlib: A 2D graphics environment, Computing in Science & Engineering, 9, 90–95, https://doi.org/10.1109/MCSE.2007.55, 2007.

Ilıcak, M., Adcroft, A. J., Griffies, S. M., and Hallberg, R. W.: Spurious dianeutral mixing and the role of momentum closure, Ocean Modelling, 45-46, 37–58, https://doi.org/10.1016/j.ocemod.2011.10.003, https://doi.org/10.1016/j.ocemod.2011.10.003, 2012.

IOC, SCOR, I.: The International thermodynamic equation of seawater–2010: calculation and use of thermodynamic properties. [includes corrections up to 31st October 2015], Intergovernmental Oceanographic Commission, Manuals and Guides Nb. 56, 2010.

Klingbeil, K., Mohammadi-Aragh, M., Gräwe, U., and Burchard, H.: Quantification of spurious dissipation and mixing – Discrete variance decay in a Finite-Volume framework, Ocean Modelling, 81, 49–64, https://doi.org/10.1016/j.ocemod.2014.06.001, https://doi.org/10.1016/j.ocemod.2014.06.001, 2014.

Lagemaa, P., Suhhova, I., Nomm, M., Pavelson, J., and Elken, J.: Comparison of current simulations by the state-of-the-art operational models in the Gulf of Finland with ADCP measurements, in: 2010 IEEE/OES Baltic International Symposium (BALTIC), IEEE, https://doi.org/10.1109/baltic.2010.5621656, https://doi.org/10.1109/baltic.2010.5621656, 2010.

Large, W. and Yeager, S.: Diurnal to decadal global forcing for ocean and sea-ice models: The data sets and flux climatologies, Tech. rep., National Center for Atmospheric Research, Boulder, Colorado, United States, https://doi.org/10.5065/D6KK98Q6, http://opensky.ucar.edu/islandora/object/technotes:434, 2004.

Lehmann, A.: A three-dimensional baroclinic eddy-resolving model of the Baltic Sea, Tellus A: Dynamic Meteorology and Oceanography, 47, 1013–1031, https://doi.org/10.3402/tellusa.v47i5.11969, https://doi.org/10.3402/tellusa.v47i5.11969, 1995.

Lemieux, J.-F., Dupont, F., Blain, P., Roy, F., Smith, G. C., and Flato, G. M.: Improving the simulation of landfast ice by combining tensile strength and a parameterization for grounded ridges, Journal of Geophysical Research: Oceans, 121, 7354–7368, https://doi.org/10.1002/2016jc012006, https://doi.org/10.1002/2016jc012006, 2016.

Lévy, M., Estublier, A., and Madec, G.: Choice of an advection scheme for biogeochemical models, Geophysical Research Letters, 28, 3725–3728, https://doi.org/10.1029/2001gl012947, https://doi.org/10.1029/2001gl012947, 2001.

Madec, G., Bourdallé-Badie, R., Chanut, J., Clementi, E., Coward, A., Ethé, C., Iovino, D., Lea, D., Lévy, C., Lovato, T., Martin, N., Masson, S., Mocavero, S., Rousset, C., Storkey, D., Vancoppenolle, M., Müeller, S., Nurser, G., Bell, M., and Samson, G.: NEMO ocean engine, https://doi.org/10.5281/zenodo.3878122, https://doi.org/10.5281/zenodo.3878122, 2019.

Meier, M., Doescher, R., Coward, A. C., Nycander, J., and Döös, K.: RCO – Rossby Centre regional Ocean climate model: model description (version 1.0) and first results from the hindcast period 1992/93, Tech. Rep. 26, SMHI, 1999.

Met Office: Iris: A Python package for analysing and visualising meteorological and oceanographic data sets, Exeter, Devon, v2.4 edn., https://scitools.org.uk/iris/docs/v2.4.0/, 2010 - 2020.

Mohrholz, V.: Major Baltic Inflow Statistics – Revised, Frontiers in Marine Science, 5, https://doi.org/10.3389/fmars.2018.00384, https://doi.org/10.3389/fmars.2018.00384, 2018.

Mohrholz, V., Naumann, M., Nausch, G., Krüger, S., and Gräwe, U.: Fresh oxygen for the Baltic Sea — An exceptional saline inflow after a decade of stagnation, Journal of Marine Systems, 148, 152–166, https://doi.org/10.1016/j.jmarsys.2015.03.005, https://doi.org/10.1016/j.jmarsys.2015.03.005, 2015.

Nemo-Nordic development team: Nemo-Nordic ocean model source code (Version 2.0), https://doi.org/10.5281/zenodo.4665840, https://doi.org/10.5281/zenodo.4665840, 2021.

O'Dea, E., Bell, M. J., Coward, A., and Holt, J.: Implementation and assessment of a flux limiter based wetting and drying scheme in NEMO, Ocean Modelling, 155, 101 708, https://doi.org/10.1016/j.ocemod.2020.101708, https://doi.org/10.1016/j.ocemod.2020.101708, 2020.

Pätsch, J., Burchard, H., Dieterich, C., Gräwe, U., Gröger, M., Mathis, M., Kapitza, H., Bersch, M., Moll, A., Pohlmann, T., Su, J., Ho-Hagemann, H. T., Schulz, A., Elizalde, A., and Eden, C.: An evaluation of the North Sea circulation in global and regional models relevant for ecosystem simulations, Ocean Modelling, 116, 70–95, https://doi.org/10.1016/j.ocemod.2017.06.005, https://doi.org/10.1016/j.ocemod.2017.06.005, 2017.

Pemberton, P., Löptien, U., Hordoir, R., Höglund, A., Schimanke, S., Axell, L., and Haapala, J.: Sea-ice evaluation of NEMO-Nordic 1.0: a NEMO–LIM3.6-based ocean–sea-ice model setup for the North Sea and Baltic Sea, Geoscientific Model Development, 10, 3105–3123, https://doi.org/10.5194/gmd-10-3105-2017, https://doi.org/10.5194/gmd-10-3105-2017, 2017.

Reffray, G., Bourdalle-Badie, R., and Calone, C.: Modelling turbulent vertical mixing sensitivity using a 1-D version of NEMO, Geoscientific Model Development, 8, 69–86, https://doi.org/10.5194/gmd-8-69-2015, https://doi.org/10.5194/gmd-8-69-2015, 2015.

Rennau, H. and Burchard, H.: Quantitative analysis of numerically induced mixing in a coastal model application, Ocean Dynamics, 59, 671–687, https://doi.org/10.1007/s10236-009-0201-x, https://doi.org/10.1007/s10236-009-0201-x, 2009.

Roquet, F., Madec, G., McDougall, T. J., and Barker, P. M.: Accurate polynomial expressions for the density and specific volume of seawater using the TEOS-10 standard, Ocean Modelling, 90, 29–43, https://doi.org/10.1016/j.ocemod.2015.04.002, https://doi.org/10.1016/j.ocemod.2015.04.002, 2015.

563   Shchepetkin, A. F. and McWilliams, J. C.: The regional oceanic modeling system (ROMS): a split-explicit, free-surface, topography-

564   following-coordinate oceanic model, Ocean Modelling, 9, 347–404, https://doi.org/10.1016/j.ocemod.2004.08.002, https://doi.org/10.

565   1016/j.ocemod.2004.08.002, 2005.

566   She, J., Berg, P., and Berg, J.: Bathymetry impacts on water exchange modelling through the Danish Straits, Journal of Marine Systems, 65,

567   450–459, https://doi.org/10.1016/j.jmarsys.2006.01.017, https://doi.org/10.1016/j.jmarsys.2006.01.017, 2007.

568   She, J., Meier, H. E. M., Darecki, M., Gorringe, P., Huess, V., Kouts, T., Reissmann, J. H., and Tuomi, L.: Baltic Sea Operational

569   Oceanography—A Stimulant for Regional Earth System Research, Frontiers in Earth Science, 8, https://doi.org/10.3389/feart.2020.00007,

570   https://doi.org/10.3389/feart.2020.00007, 2020.

571   Stanev, E., Pein, J., Grashorn, S., Zhang, Y., and Schrum, C.: Dynamics of the Baltic Sea straits via numerical simulation of exchange flows,

572   Ocean Modelling, 131, 40–58, https://doi.org/10.1016/j.ocemod.2018.08.009, https://doi.org/10.1016/j.ocemod.2018.08.009, 2018.

573   Taylor, K. E.: Summarizing multiple aspects of model performance in a single diagram, Journal of Geophysical Research: Atmospheres, 106,

574   7183–7192, https://doi.org/10.1029/2000jd900719, https://doi.org/10.1029/2000jd900719, 2001.

575   Umlauf, L. and Burchard, H.: A generic length-scale equation for geophysical turbulence models, Journal of Marine Research, 61, 235–265,

576   https://doi.org/10.1357/002224003322005087, https://doi.org/10.1357/002224003322005087, 2003.

577   Vancoppenolle, M., Fichefet, T., Goosse, H., Bouillon, S., Madec, G., and Maqueda, M. A. M.: Simulating the mass bal-

578   ance and salinity of Arctic and Antarctic sea ice. 1. Model description and validation, Ocean Modelling, 27, 33–53,

579   https://doi.org/10.1016/j.ocemod.2008.10.005, https://doi.org/10.1016/j.ocemod.2008.10.005, 2009.

580   Zalesak, S. T.: Fully multidimensional flux-corrected transport algorithms for fluids, Journal of Computational Physics, 31, 335–362,

581   https://doi.org/10.1016/0021-9991(79)90051-2, https://doi.org/10.1016/0021-9991(79)90051-2, 1979.